1

A mathematical model for irrigated epicardial radiofrequency ablation

Jayadeep Gopalakrishnan

Abstract— **A mathematical model for epicardial radiofrequency ablation using an electrode irrigated by saline is proposed. Saline flow profiles are derived using thin film theory, and heat convection due to blood flow is also included in the model. Results from a computer implementation of the model using a finite element method suggest that transmural RF ablation lesions can be made in 4 mm thick tissue. Effects of parameters such as tissue and saline layer thickness, irrigation rate, blood flow rate, and applied power are investigated. Saline is found to irrigate as well as ablate. Rise in saline temperature and consequent ablation by saline is more pronounced as saline layer becomes thicker. Electrode tip temperatures as much as 40 ℃ lower than maximum tissue temperature were found in simulations.**

Keywords— **arrhythmia, radiofrequency, invasive, epicardial, ablation, irrigation, saline, irrigated electrode, Joule heating, thin film, numerical model, finite element**

I. Introduction

During the last decade, radiofrequency ablation has emerged as a preferred alternative to drug therapy for treating certain supraventricular arrhythmias. Design of ablation electrodes has therefore become an active subject of research. Electrodes commonly called "pen electrodes" have been used for epicardial ablation [13]. This paper presents a mathematical model for irrigated pen electrodes (similar to Cardioblate, Medtronic Inc., Minneapolis).

At present, commonly used ablation techniques are endocardial. These typically involve advancing an electrode mounted on the distal end of a catheter via a vein until an endocardial location needing ablation. Epicardial ablation, on the other hand, is usually more invasive. It involves a transthoracic opening to the pericardium and exposing the heart. An ablation electrode is then placed on the epicardial location needing ablation, and radiofrequency energy applied until a lesion of required dimensions is created.

Despite its invasive nature, epicardial ablation is an important alternative. Epicardial ablation permits clear view of ablating area. Unlike endocardial ablation, it avoids electrode-blood contact which is known to increase the risk of thromboembolic stroke [16]. It is believed that a part of reentrant circuit in some ischemic ventricular tachycardias is located in a subepicardial layer of cardiac muscle that is difficult to ablate using endocardial catheter techniques [26]. Epicardial maze procedures have been very successful in patients without contraindications to surgery [3], and recent studies indicate that ablation can eliminate the need for sewing in maze procedure [13].

Few studies exist on design of epicardial electrodes. In contrast, endocardial ablation is thoroughly studied: Successful numerical models have been proposed and experimentally validated [6], [14], [15], [20] in this case. However, no numerical model for irrigated epicardial ablation has been proposed yet (see [9] for a study without irrigation).

Epicardial ablation can be performed on either a beating or a stopped heart. It is a particularly interesting alternative in the former case as cardiopulmonary bypass is avoided. Our model is aimed at this case. Consequently, we must take into account cooling due to endocardial blood flow in the model. We must also take into account cooling due to saline emission from pen electrode (see Fig. 1).

Irrigation is more important in the case of epicardial ablation than endocardial ablation. In contrast to endocardial ablation, during epicardial ablation, the electrode is not cooled by blood flow. Moreover, due to the smaller electrode contact surface area, impedance of the ablation system is higher. Therefore, without irrigation, temperature of the system will rise rapidly to 100 ℃ (beyond which tissue usually pops) resulting in a failed procedure. Ideally, in an ablation procedure, one wants the ability to create as large a lesion as possible. Keeping in view the fact that myocardium becomes nonviable at 50 ℃, this means that the system should have as large a region as possible above 50 ℃ but not above 100 ℃. Irrigation helps in achieving this by taking heat away from some hot spots.

Irrigation in pen electrode differs from irrigation in endocardial electrodes. The flow rate of saline in the former is much lower than that in the latter. While saline mixes with blood and is carried away immediately in the latter case, in epicardial ablation it oozes out of the electrode and forms a film of flowing saline on the electrode and epicardial surfaces.

There are no models of irrigated epicardial ablation in the literature. We construct a new numerical model by deriving a flow profile of irrigating saline using a thin film flow approximation, and incorporating it into a finite element model. We include heat loss due to blood flow into the model explicitly, in contrast to most of the previous models wherein it is approximated either as a boundary condition [15] or as a heat-sink term [20]. Models with flow fields have appeared only recently [11]. We clarify the numerical difficulties in incorporating high blood flow into a finite element model and show how to overcome them.

An important issue in the design of electrodes is placement of temperature sensors to monitor electrode temperature during ablation. It is known [19], [29] that in saline cooled endocardial ablation, electrode temperature signifi-

This work was initiated when the author was with Institute for Mathematics and its Applications, University of Minnesota, Minneapolis. His current address is Department of Mathematics, University of Florida, Gainesville, FL 32611–8105. E-mail: jayg@ima.umn.edu. Telephone: (352) 392-0281. Fax: (352) 392-8357.

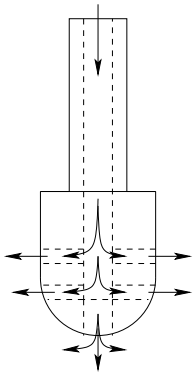

Fig. 1. Schematic of irrigation in a pen electrode.

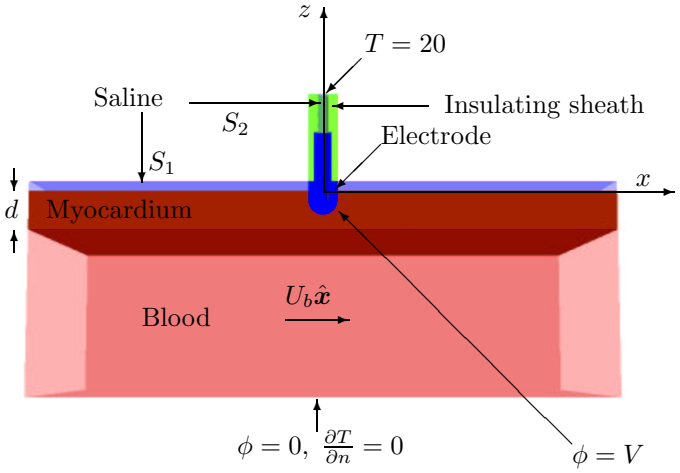

Fig. 2. Computational domain.

cantly underestimates maximum tissue temperature (only the former can be monitored). This, and other electrode design issues are investigated further in Sections IV and V. There, we will also attempt to answer a fundamental question: Can one create a transmural lesion using pen electrodes?

II. Numerical model and methods

A mathematical model for ablating cardiac tissue can be constructed using the principles of Joule heating and quasistatic electric field approximations. Such models have previously been investigated [6], [10], [14], [15], [18], [20]. In this section, a model with explicit convective heat loss terms is presented, together with a strategy for numerical solution.

The electric field $\boldsymbol{E}(x, y, z)$ generated by an ablation electrode can be approximated by $\boldsymbol{E} = \boldsymbol{\nabla}\phi$, where ϕ satisfies

$$\nabla \cdot (\sigma \boldsymbol{\nabla}\phi) = 0. \tag{1}$$

Here σ is electrical conductivity. According to the Joule heating principle, temperature $T(t, x, y, z)$ satisfies

$$\rho c \frac{\partial T}{\partial t} = \nabla \cdot (\kappa \boldsymbol{\nabla} T) + \sigma \boldsymbol{\nabla}\phi \cdot \boldsymbol{\nabla}\phi - \rho c\, \boldsymbol{v} \cdot \boldsymbol{\nabla} T. \tag{2}$$

	ρ kg/mm^3	c J/kg/°C	σ S/mm	κ W/mm/°C
Blood	1.00e–6	4180	9.95e–4	5.43e–4
Myocardium	1.20e–6	3200	6.10e–4	7.00e–4
Electrode	2.15e–5	132	4.00e+3	7.10e–2
Saline	0.98e–6	4184	1.35e–3	6.28e–4
Insulator	7.00e–8	1045	1.00e–8	2.60e–5

TABLE I
Material properties

The last term represents heat loss due to blood flow and saline irrigation, and $\boldsymbol{v}(x, y, z)$ denotes a time-averaged flow velocity field. In (2), κ is the thermal conductivity, ρ is mass density, and c is specific heat capacity. The material properties that are used in our simulations are the same as that used in an earlier work [14] and are tabulated in Table I.

The computational domain consists of a rectangular box ($60 \times 60 \times 20$ mm) of flowing blood, on top of which is myocardial tissue of thickness d mm and a saline film of thickness 1/2 mm (see Fig. 2). Current is delivered by maintaining a voltage V at an electrode partially embedded in tissue. The length of the embedded part of the electrode is 2.5 mm. The electrode consists of a hemispherical tip, an adjacent cylindrical part of radius 1.5 mm, and a remainder sheathed in an insulator. The radius of the electrode and the thickness of saline layer set above are typical values observed in prototypical pen electrodes. Voltage is set to zero at the bottom surface of the model. At other exterior surfaces, an electrical boundary condition of $\partial\phi/\partial n = 0$ is imposed. Only half the actual domain is modeled due to a plane of symmetry. The origin, as shown in Fig. 2, is such that the saline-tissue interface is in the x–y-plane, and z-axis aligns with the axis of the electrode. This model does not contain a fat layer, because the epicardial fat layer is typically removed surgically before ablation.

Initially (at time $t = 0$), the entire system is at the ambient body temperature $T_a = 37\,$°C, except the saline and electrode regions which are at room temperature $T_r = 20\,$°C. Saline flow is usually turned on before ablation, so electrode is at saline temperature rather than body temperature. On the saline inflow boundary (top of region S_2 in Fig. 2) the condition $T = 20\,$°C is maintained at all time. On surfaces exposed to air, a free convective boundary condition of the form $\kappa\partial T/\partial n = \alpha(T - T_r)$ may be appropriate. However, values of α of natural convection [2] are negligible. Therefore, a zero thermal flux boundary condition is applied at these surfaces. The same boundary condition is also applied at all exterior model boundaries, except the blood inflow boundary where $T = 37\,$°C at all times.

We are modeling an electrode with an open irrigation system. The electrode has a cylindrical hole (see region S_2 in Fig. 2) for saline flow running from its top end until 1.5 mm from its tip. In reality this type of electrode will

also have lateral saline flow channels (and a channel extending to the tip) that emit saline out (as in Fig. 1). This has been excluded in our model for the sake of simplicity (see also Section V). A complete numerical model with all irrigation channels is possible, but would require more complex numerical techniques for computing fluid velocity profiles. Our intention is to arrive at a simple analytically given approximation of the complex flow.

The velocity vector field $\boldsymbol{v}(x, y, z)$ in (2) is set as follows (see Section III):

$$\boldsymbol{v} = \begin{cases} \dfrac{6Q}{\pi r}(z - z^2)\hat{\boldsymbol{r}}, & \text{in saline layer } S_1; \\ U_b\,\hat{\boldsymbol{x}}, & \text{in blood;} \\ \mathbf{0}, & \text{elsewhere.} \end{cases} \tag{3}$$

Here $\hat{\boldsymbol{r}}$ is the unit radial vector in cylindrical coordinates, $\hat{\boldsymbol{x}}$ is the unit vector in x-direction, and Q is saline flow rate. The velocity profile in S_1 given above will be derived theoretically in Section III. Although in reality, saline flows in region S_2 as well, in our model the saline is stationary there. Numerical experiments with a velocity profile corresponding to a Poiseuille pipe flow (for typical flow rates) set in S_2 gave results that did not differ significantly with the case of stationary saline. This justifies setting zero flow in S_2. Blood flow speed is assumed to be a constant U_b.

Equations (1) and (2) are solved numerically using finite elements. The standard finite element method is not appropriate for solving (2), as it is unstable for convection dominated problems [12]. A scaling analysis reveals that (2) indeed represents a convection dominated problem: Equation (2), when restricted to the region of flowing blood, in terms of nondimensional quantities $(\hat{x}, \hat{y}, \hat{z}) = (x, y, z)/L$ and $\hat{\boldsymbol{v}} = \boldsymbol{v}/U_b$, becomes

$$\frac{L}{U_b}\frac{\partial T}{\partial t} = \varepsilon\hat{\Delta}T - \hat{\boldsymbol{v}}\cdot\hat{\boldsymbol{\nabla}}T + \frac{\sigma}{\rho c L U_b}|\hat{\boldsymbol{\nabla}}\phi|^2,$$

where $\varepsilon = \kappa/\rho c L U_b$, and operators $\hat{\Delta}$ and $\hat{\boldsymbol{\nabla}}$ are Laplacian and gradient in the nondimensional variables $\hat{x}, \hat{y}, \hat{z}$. For typical values of material properties [14], length scale ($L = 50$ mm), and blood velocity ($U_b = 10^3$ mm/s), the nondimensional diffusion coefficient ε is of the order of 10^{-6}, indicating a convection dominated problem. The streamline diffusion finite element method, on the other hand, is a method well suited for convection dominated problems [12]. Therefore, this is employed for solving (2). For solving (1), the standard finite element method will suffice.

First, we set $d = 4$, and create a tetrahedral mesh of the domain with 70884 vertices and 386375 elements using NETGEN (research version) [23]. We also tested cases $d = 6$ and $d = 8$ with 396519 and 552126 elements respectively. A mesh size of at most 1/4 mm was ensured in regions within 8 mm of the electrode. Linear finite elements are used. The backward Euler implicit time discretization is used to discretize (2) in time, with uniform time-steps of 10^{-2} s. Iterative techniques are employed to solve resulting finite element systems. For computation of electric potential, the conjugate gradient method [7] is used, but since (2) can give rise to a nonsymmetric system, GMRES [22] is used for temperature calculation.

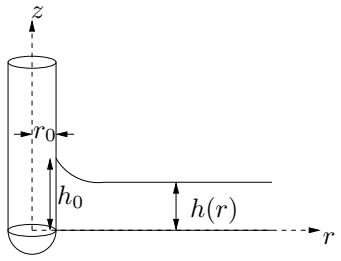

Fig. 3. A film of saline flowing radially away from electrode.

III. Saline velocity field

We now use the theory of thin films to derive a velocity field for the saline flowing out of electrode pores, thus theoretically justifying the use of flow field (3) in the computational model. Our approach is inspired by similar arguments used in [8] for lava flows.

The steady axisymmetric laminar flow of saline can be described by Navier-Stokes equations for incompressible flow in cylindrical coordinates:

$$\frac{1}{r}\frac{\partial(ru)}{\partial r} + \frac{\partial v}{\partial z} = 0, \tag{4}$$

$$\frac{1}{\rho}\frac{\partial p}{\partial r} = \nu\left(\frac{1}{r}\frac{\partial}{\partial r}r\frac{\partial u}{\partial r} + \frac{\partial^2 u}{\partial z^2} - \frac{u}{r^2}\right), \tag{5}$$

$$\frac{1}{\rho}\frac{\partial p}{\partial z} = \nu\left(\frac{1}{r}\frac{\partial}{\partial r}r\frac{\partial v}{\partial r} + \frac{\partial^2 v}{\partial z^2}\right) + g, \tag{6}$$

where $u(r, z)$ and $v(r, z)$ are the r- and z-components of the velocity field respectively, p is pressure, ν is kinematic viscosity, and g is acceleration due to gravity. These equations hold in the region of flowing saline given by $r > r_0$ and $0 < z < h(r)$ (shown in Fig. 3). Let H and R be characteristic depth and length of the saline layer, and let U be characteristic saline flow speed. Under two standard assumptions of thin film theory, (5) and (6) can be simplified (see e.g. [1]):

1. $H/R \ll 1$, i.e., the film of saline is thin; and
2. $UH^2/\nu R \ll 1$, i.e., the flow rate is small.

For typical values $H = 1$ mm, $R = 50$ mm, $\nu = 1$ mm^2/s, and $Q = 30$ mm^3/s (corresponding U being $Q/2\pi r_0 H$ mm/s), the dimensionless numbers H/R and $UH^2/\nu R$ are of the order of 10^{-2}, so these assumptions hold.

Equations (5) and (6) when non-dimensionalized, and expanded asymptotically in H/R and $UH^2/\nu R$, yields the first order approximation

$$\frac{1}{\rho}\frac{\partial p}{\partial r} = \nu\frac{\partial^2 u}{\partial z^2}, \quad \text{and} \tag{7}$$

$$\frac{1}{\rho}\frac{\partial p}{\partial z} = -g. \tag{8}$$

Equations (4), (7), and (8) form three equations for the three unknowns $u(r, z)$, $v(r, z)$, and $p(r, z)$. The height of

the free boundary $h(r)$ is also an unknown, so we must include more equations. Since particles on the free boundary continue to remain on it,

$$uh' - v = 0, \quad \text{on } z = h(r). \tag{9}$$

We use primes denote differentiation with respect to r, e.g., $h' = dh/dr$. In addition to (9), the fact that tangential stresses at the free surface are zero, under the thin film approximation gives

$$\frac{\partial u}{\partial z} = 0, \quad \text{on } z = h(r). \tag{10}$$

The flow rate Q, initial height of the free surface h_0, and atmospheric pressure p_0, are given. This gives the constraints

$$h(r_0) = h_0, \tag{11}$$

$$2\pi r_0 \int_0^{h_0} u(r_0, z)\, dz = Q, \quad \text{and} \tag{12}$$

$$p(r, h(r)) = p_0. \tag{13}$$

Finally, the no-slip condition must also be satisfied, so

$$u(r, 0) = v(r, 0) = 0. \tag{14}$$

We will now explicitly calculate a solution for the system of equations (4), (7), (8), (9), (10), (11), (12), (13), and (14). Equation (8) can be integrated using (13) to yield

$$p(r, z) = p_0 + \rho g(h(r) - z). \tag{15}$$

Now, by integrating (7) twice, with (10) and (14) as boundary conditions, we get

$$u(r, z) = \frac{\rho g}{\mu} h'(r) \left(\frac{z^2}{2} - h(r)z\right). \tag{16}$$

From the continuity equation (4) it follows that

$$v(r, z) = \frac{\rho g}{\mu} \left(h'(r)^2 \frac{z^2}{2} - \frac{(h'(r)r)'}{r} \left(\frac{z^3}{6} - h(r)\frac{z^2}{2}\right)\right). \tag{17}$$

To calculate $h(r)$, we use the kinematic condition (9) wherein the expressions for u and v computed above are substituted. After simplifications, (9) reduces to $(rh^3h')' = 0$. This equation can be solved for $h(r)$ (also using (11) and (12)) to get

$$h(r) = \left(h_0^4 - \frac{6\nu Q}{\pi g h_0} \ln \frac{r}{r_0} \right)^{1/4}. \tag{18}$$

Thus we have found all the functions involved in the model.

Let us now set $h_0 = 0.5$ mm, $r_0 = 1.5$ mm to match the setup of Section II. Equation (4) implies that $v(r, z)$ is an order of magnitude less than $u(r, z)$. Since $u(r, z)$ is quadratic in z, for each fixed r, the flow profile is approximately parabolic (see Fig. 4). For typical values of Q used in pen electrodes, the function $h(r)$ does not vary greatly. Indeed for $Q \le 80$ mm^3/s, in the range $r_0 \le r \le 10r_0$,

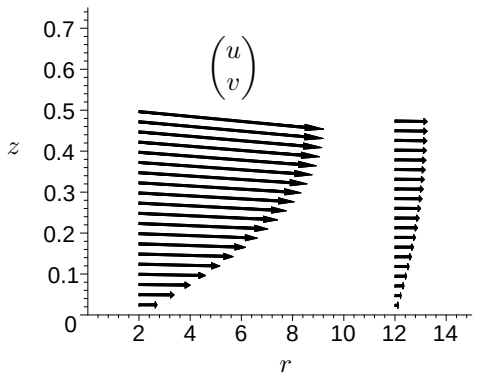

Fig. 4. Flow profiles given by (16) and (17) at $r = 2$ and 12 mm, when $Q = 30$ mm^3/s.

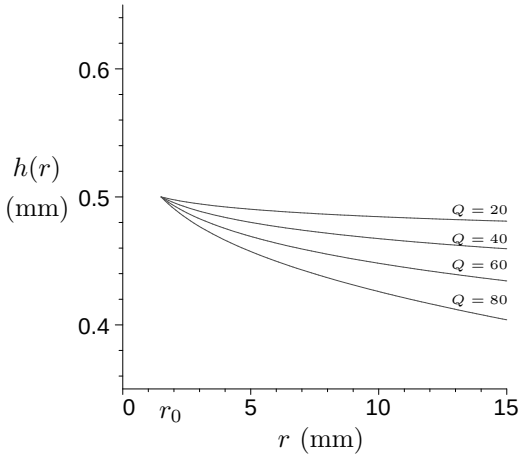

Fig. 5. The slight variation of $h(r)$ with r for various flow rates.

we have $0.4 \le h(r) \le 0.5$ (see Fig. 5). Thus, the free surface may be considered flat to a good approximation, i.e., $h(r) \approx h_0$.

The saline free surface given by (18) is difficult to incorporate in computations using available finite element tools. Since $h(r) \approx h_0$, in our finite element model, we set a saline layer of uniform thickness $h_0 = 0.5$ mm. We must now find a way to approximate the velocity field consistent with this setting. Observe that (16) can be rewritten as

$$u(r, z) = \frac{3Q}{2\pi r h^3}\left(zh - \frac{z^2}{2}\right). \tag{19}$$

Since $h(r) \approx h_0$, this suggests approximating $u(r, z)$ by

$$u_0(r, z) = \frac{3Q}{2\pi r h_0^3}\left(zh_0 - \frac{z^2}{2}\right). \tag{20}$$

The relative error in such approximation can be estimated by

$$\left|\frac{u - u_0}{u}\right| \le \left|1 - \frac{h^3}{h_0^3}\right|,$$

which gives a 17% error for $r_0 \le r \le 10r_0$ and $Q = 30$ mm^3/s. Note that the error decreases near the electrode. This error should not be taken as a measure of error

in temperature calculation. In fact, it can be mathematically proven that the temperature error depends on the product of the error in velocity field and the gradient of the original temperature distribution. Since temperature gradients are small away from the electrode, the approximation therefore need only be accurate near the electrode. For these reasons, the use of the saline velocity profile of (3) in our model is justified.

Finally, note that (20) can be derived directly by assuming that velocity field (u, v) has the form

$$u(r, z) = (az^2 + bz + c)f(r),$$

and $v = 0$. The undetermined constants a, b and c, and function f, can be computed and (20) recovered using (4), (10), (12), and (14). Thus, the velocity profile can be considered to hold even when the thin film approximations fail, provided the above assumption of quadratic dependence on z holds.

IV. Results

We now present results from computer simulation of the model with typical values of parameters, and discuss variations with respect to parameters d, V, Q and U_b. For any simulation, let $t_{\max}$ denote the time at which some point in the tissue reaches 100 ℃. Computations are shut down at time $t_{\max}$, as we have not modeled the change in physical properties that accompanies popping and char formation associated with a temperature greater than 100 ℃.

First, consider the model with $d = 4$ mm, $V = 35$ V, $Q = 80$ mm^3/s, $U_b = 500$ mm/s. The impedance of the model was 93.2 Ω, so the voltage setting implies a constant power supply of 13.1 W. In this case, $t_{\max}$ was found to be 9.6 s. Temperature profile at this time and electric potential are given in Figures 6 and 7 respectively. We mark a tissue mesh element ablated if its vertex temperatures are higher than 50 ℃. The ablated region obtained is shown in Fig. 13. (Vertices on the endocardial surface often do not achieve 50 ℃, due to numerical errors and absence of a fluid boundary layer in the blood region in our model. Therefore, if the boundary of ablated region is within one mesh element of the endocardial surface, we consider the lesion to be transmural.) We find that a transmural lesion can be created in this case. The shape of the ablated region is similar to lesion shapes obtained in irrigated endocardial ablation [19].

Values of temperature at points A, B, C, and D marked in Fig. 8 as a function of time are plotted in Fig. 9. We find that tip temperature (T_{B}) is consistently lower than temperature further below at A (T_{A}). However T_{B} can be used to monitor rise in T_{A} as $T_{\mathrm{A}} - T_{\mathrm{B}}$ after 5 seconds varied less than 2.5 ℃. Note also that the point C has almost the same temperature-time graph as the tip B. Thus, C is an alternate location for a temperature sensor. Indeed, many points near the tip of the electrode were found to possess almost identical temperature-time graphs. This appears to be in contrast to ablation without irrigation wherein edge effects have to be considered in sensor placement [17].

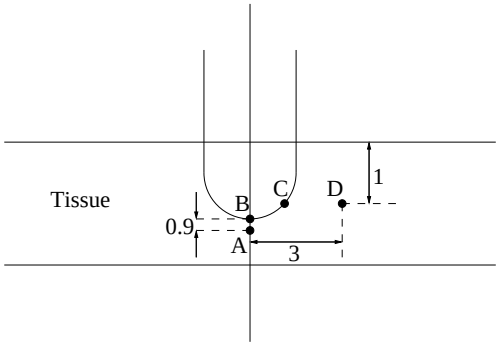

Fig. 8. Points where temperature is probed. (Drawing is to scale, points are in the $y = 0$ plane, and distances marked are in mm.)

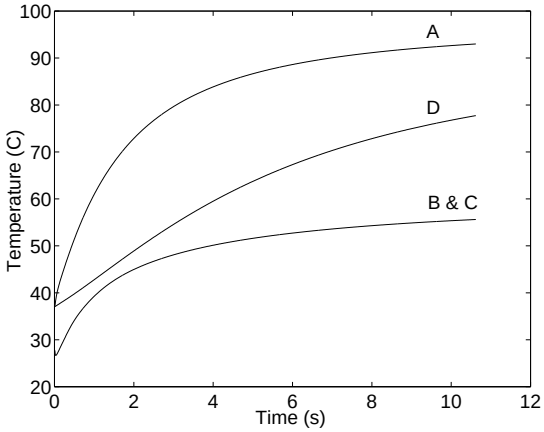

Fig. 9. Temperatures at points A, B, C, and D marked in Fig. 8. ($d = 4$ mm, $V = 35$ V, $Q = 80$ mm^3/s, $U_b = 500$ mm/s.)

Ablated volume increased when blood speed U_b was increased, as shown in Table II. However, the increase is not large. This is in contrast to the case of endocardial ablation, where blood velocity seems to be a significant factor [11], [28]. Unlike endocardial ablation, blood flow in epicardial ablation can only convect heat conducted to the endocardial surface. This explains why blood flow has smaller impact in epicardial ablation. Note that there was a slight increase in the temperature of blood downstream as shown in Fig. 6 for lower blood velocities.

Variation of ablated volume with flow rate Q is shown in Fig. 10. There was a slight increase in ablated volume with increase in flow rates. We did not run simulations with flow rates beyond 100 mm^3/s because the thin film approximation upon which we based our model breaks down at such flow rates (see assumptions of Section III).

Significant differences in ablated volume are observed when power delivered is reduced, as seen from Fig. 11. Lesions widen laterally at lower power settings. Longer time is required for the system to achieve 100 ℃ in this case, as seen in Fig. 12. In other words, an increase of power brings about rapid ablation, but need not result in larger lesion volumes. Tip temperatures, and temperatures at A at various times are given in Fig. 14.

We now consider ablation of thicker tissues. The above

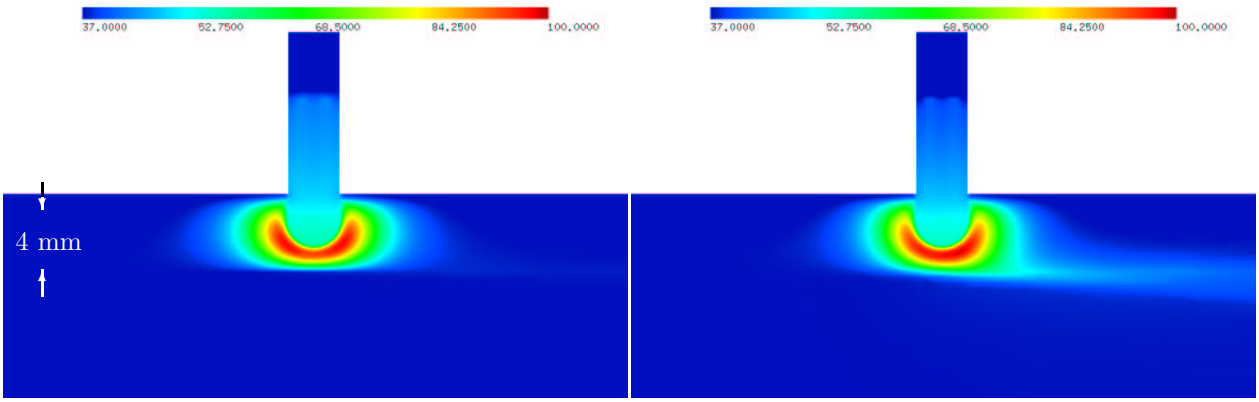

Fig. 6. Final temperature profiles (on slice $y = 0$). Left profile shows the case of blood velocity $U_b = 500$ mm/s, and right profile that of $U_b = 10$ mm/s. (Blood flow is to the right, $d = 4$ mm, $V = 35$ V, and $Q = 80$ mm^3/s.)

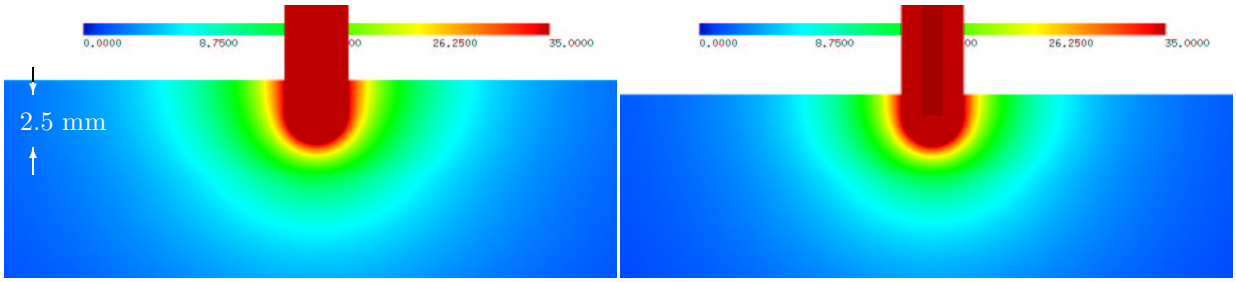

Fig. 7. Electric potential with and without irrigation. (Here $d = 4$ mm, $V = 35$ V, and slice $y = 0$ is shown.) Right profile shows the case without irrigation, so the saline regions S_1 and S_2 are absent there.

U_b (mm/s)	$t_{\max}$ (s)	Ablated volume (mm^3)
0	5.3	136
10	7.2	161
50	9.1	171
100	9.3	169
500	9.6	169
1000	9.7	168

TABLE II
VARIATION OF ABLATED VOLUME WITH BLOOD VELOCITY

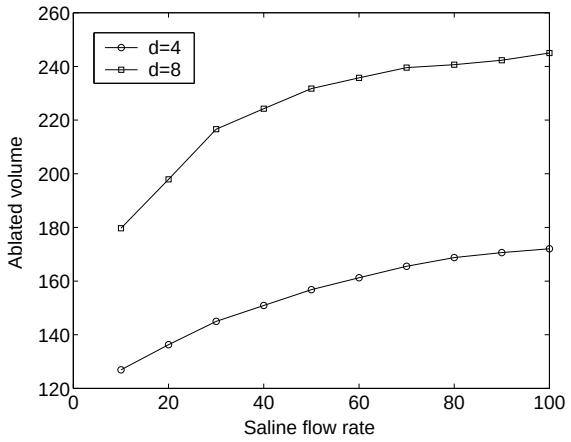

Fig. 10. Ablated volume (mm^3) as a function of flow rate Q (mm^3/s). (Here $V = 35$ V and $U_b = 500$ mm/s.)

simulations are repeated with $d = 8$ (where d is as in Fig. 2). Graphs labeled $d = 8$ in Figures 10, 11, and 12 show the results. Clearly, higher lesion volumes are obtained. However, the lesion obtained with $V = 35$ V was not transmural (see Fig. 13).

V. Discussion

Temperature sensing in irrigated electrodes is known to be difficult [19], [29]. As seen from Fig. 14, electrode tip temperature T_B is 40 ℃ lower than temperature at a deeper location T_A in some simulations. However, in all our simulations, $T_A - T_B$ never exceeded 2.5 ℃ after 5 s. This suggests that rise in temperature of deeper tissue can be monitored using tip temperature.

Although the temperatures at A, B and C plateaus near time $t_{\max}$, the temperature at D continues to rise (see Fig. 9). Temperature at D is difficult to sense in practice. Thus, in clinical use, it should not be assumed that a steady state has been reached merely because readings from a sensor at electrode tip do not rise. Another implication of this finding is that if we continued power delivery beyond $t_{\max}$ we can create larger lesions, provided popping does not occur.

Because saline has higher conductivity than adjacent tissue, the isoelectric lines (and consequently current density)

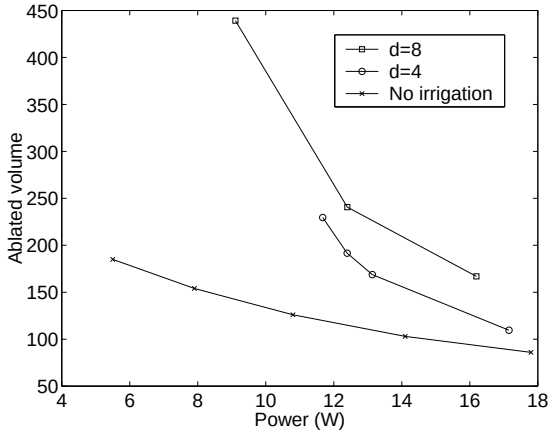

Fig. 11. Ablated volume (mm^3) as a function of power delivered ($Q = 35$ mm^3/s, $U_b = 500$ mm/s).

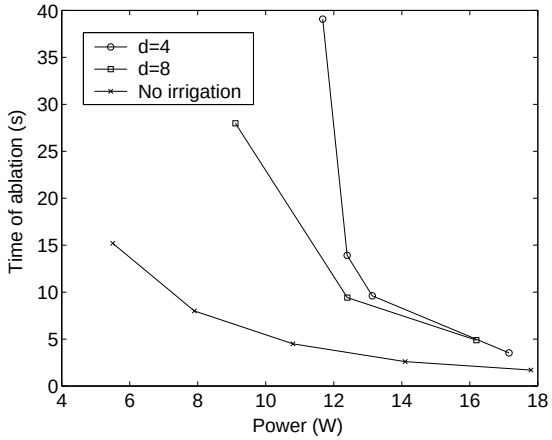

Fig. 12. Time of ablation ($t_{\max}$) vs. power. ($Q = 80$ mm^3/s, $U_b = 500$ mm/s.)

Fig. 13. Ablated regions ($V = 35$ V, $Q = 80$ mm^3/s, $U_b = 500$ mm/s).

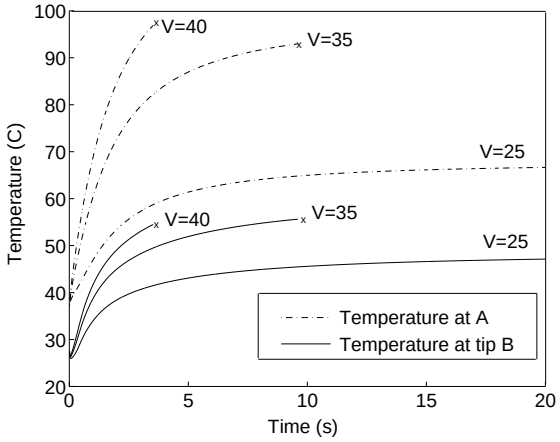

Fig. 14. Temperatures at A and B for different power settings. (Here $d = 4$ mm, $Q = 80$ mm^3/s, and $U_b = 500$ mm/s. An "x" indicates that system reached 100 ℃.)

Fig. 15. Ablated region obtained with a thicker saline layer ($V = 35$ V, Power= 15.3 W, $Q = 80$ mm^3/s, $U_b = 500$ mm/s).

extend farther from the electrode in the presence of saline than without it (see Fig. 7). The presence of saline thus appears to facilitate ablation of a larger area. In connection with endocardial irrigation, this phenomenon (often called "virtual electrode effect") is not considered significant [21]. Perhaps it is less pronounced there, as the irrigating saline mixes with blood and is carried away from the vicinity of the electrode faster. Note also that saline can achieve higher temperatures when flow rate is low. E.g., the case $Q = 10$ mm^3/s resulted in saline temperatures higher than 65 ℃ near electrode, in contrast to the $Q = 30$ mm^3/s case depicted in Fig. 6. Thus, saline can get hot enough to ablate the tissue beneath it by conduction.

Interestingly, the shape of the ablated region changes if we set the saline layer thickness to be 1 mm (instead of 0.5 mm). The lesion obtained in this case, as shown in Fig. 15, has beveled lips near saline. In this simulation, saline near the electrode attained temperatures as high as 70 ℃, and ablated tissue beneath it by conduction. As saline thickness increases, more heat is generated within saline by resistive heating. Moreover, (19) implies that for any given flow rate, thicker saline layer implies reduced flow speed, and consequently reduced convective cooling by saline. In practical use, myocardial tissue often makes a dimpled region near the electrode due to the electrode pushing into it. When the dimple is deep, saline forms a slow flowing pool in this region and a thick saline layer re-

sults. Then, lesions as in Fig. 15 may be created. Clearly, ablation of tissue by saline is more pronounced in this situation.

We have seen that saline ablates. To verify the often made claim that saline irrigates, i.e, to verify that the convective cooling of saline is significant, simulations were carried out after removing saline from the model. (Blood flow was retained, so the model does have some convective heat losses.) Then the impedance of the model increased to 114 Ω. Resulting simulations gave rise to smaller ablated volumes, as shown in Fig. 11. Temperature increased more rapidly as seen in Fig. 12, confirming that saline indeed convects heat away. Similar experimental observations have been made in the case of endocardial ablation [19], [25].

The importance of being able to create linear transmural lesions in treatment of atrial fibrillation is well known [3]. Since atrial walls are usually not thicker than 4 mm, the fact that we could create a transmural lesion in the case $d = 4$, even with high blood velocity, supports the use of pen electrode on a beating atrium.

On the other hand, the fact that we could not obtain a transmural lesion in the case $d = 8$ suggests that more studies are needed before the pen electrode can be used for ablation of thick ventricular walls adjacent to high blood flow. Ventricular walls are thicker than 8 mm at various locations.

We should note that lesions can grow larger and become transmural under prolonged low power exposure. This situation is clearer in the case $d = 6$, with Q and U_b set to 80 mm^3/s and 10 mm/s respectively. Simulations in this case, with $V = 35$ V, i.e., with a constant power setting of 12.6 W, did not yield a transmural lesion (at time $t_{\max} = 8.2$ s). However, when the power setting was lowered to 6.4 W, the simulated ablation process continued past 10 minutes (without the system reaching 100 ℃). At this time the lesion was already transmural (cf. experimental studies in [25]).

VI. Limitations

Limitations of this study arise not only from the fact that a careful experimental validation of the model is yet to be conducted, but also because of several unmodelled features. The qualitative behavior of the model, including lesion shapes obtained, agrees with what is generally observed in practice. A few comments on the unmodelled features are in order.

The pen electrode, as indicated in Fig. 1, has lateral flow channels, that we did not include in the model. As pointed out earlier, when a Poiseuille pipe flow field was set in irrigation channel S_2 the simulation results were hardly altered (temperatures probed changed by less than 1%). This indicates that ignoring flow in other channels will not change our results.

We have neglected boundary layers in blood flow. Little data was found in literature on velocity profile near cardiac walls, probably due to the difficulty in measurements caused by movement of heart. In any case, as we have seen, our model did not exhibit severe variations with respect to blood speed. Therefore, we expect our simulation results not to change significantly if a more realistic velocity profile is substituted.

Other features we have neglected include metabolic heat generation, perfusion losses, and temperature dependence of material properties. It is well known [20] that these are indeed negligible. Heat losses due to blood flow in coronary arteries are also neglected. This will need to be taken into account in ablation near big vessels, especially in ventricles. In clinical use, the electrode is often moved back and forth to create a linear lesion. This is difficult to include in our model, as is movement of a beating heart.

Our ablation times and lesion volumes are conservative estimates. We shut down simulations when any point in the modeled tissue reaches 100 ℃. We are thus ignoring time needed to accumulate latent heat required for steam formation and ensuing popping observed in practice. One other factor to be considered in longer pen electrodes is that saline oozes out of higher irrigation holes and forms a saline film on electrode surfaces (as well as the tissue surface). This reduces the impedance of the system, and increases cooling of the electrode, permitting longer ablation times.

Our results should be considered qualitatively rather than quantitatively, due to large variations in material properties of human myocardium reported in literature (cf. [4], [5], [24], [27]). The results are sensitive to changes in σ. E.g., if material properties from [18], [20] are used in the simulation with $d = 4$, $V = 35$, $Q = 80$, $U_b = 500$, impedance rises to 180.7 Ω, so power consumed is only 6.8 W, and ablated volume and ablation time are larger. Clearly, without more precise information on material properties it is not possible to make quantitative predictions with any numerical model. However, we found that the qualitative behavior of the model remains unaltered. Furthermore, the conclusions enumerated in the next section remain true even when material properties from [20] are substituted for those in Table I.

VII. Conclusions

A new model for saline irrigated pen type electrodes for epicardial ablation was proposed. Numerical experiments with the model give physically sound results. Our findings suggest the following:

1. The epicardial pen electrode yield transmural lesions in 4 mm thick tissue, in spite of convective heat losses due to blood flow.
2. Saline in epicardial ablation irrigates as well as ablates. Ablation by saline is more pronounced when saline film is of thickness 1 mm than when it is 1/2 mm thick. This suggests that ideal lesion shapes may not be obtained if saline is allowed to form thick stagnant pools near the electrode.
3. Temperature at electrode tip can be as much as 40 ℃ lower than maximum temperature. However, rise in temperature of tissue at deeper locations can be monitored using rise in electrode tip temperature.

Acknowledgments

This work was supported partly by Medtronic Inc., 7000 Central Ave. NE, Minneapolis. The author wishes to thank F. Santosa for facilitating industrial contacts that made this work possible, D. J. Kirill for discussions on thin films, D. Francischelli for critiquing the manuscript, and the anonymous referees for many valuable suggestions.

References

[1] D. J. Acheson. *Elementary fluid dynamics*. The Clarendon Press, Oxford University, New York, 1990.

[2] C. O. Bennet and J. E. Myers. *Momentum, Heat and Mass Transfer*. McGraw Hill, New York, second edition, 1974.

[3] James L. Cox, John P. Boineau, Richard B. Schuessler, Kathryn M. Kater, and Demetrios G. Lappas. Five-year experience with the maze procedure for atrial fibrillation. *Ann. Thorac. Surg.*, 56:814–824, 1993.

[4] Francis A. Duck. *Physical properties of tissue: a comprehensive reference book*. Academic Press, San Diego, 1990.

[5] Camelia Gabriel. Compilation of the Dielectric Properties of Body Tissues at RF and Microwave Frequencies. Technical Report AL/OE-TR-1996-0037, Armstrong Laboratory, Brooks airforce base, TX, 78235-5102, 1996.

[6] D. E. Haines and D. D. Watson. Tissue heating during radiofrequency catheter ablation: a thermodynamic model and observations in isolated perfused and superfused canine right ventricular free wall. *Pacing. Clin. Electrophysiol.*, 12(6):962–976, June 1989.

[7] Magnus R. Hestenes and Eduard Stiefel. Methods of conjugate gradients for solving linear systems. *J. Research Nat. Bur. Standards*, 49:409–436, 1952.

[8] Herbert E. Huppert. The propagation of two-dimensional and axisymmetric viscous gravity currents over a rigid horizontal surface. *J. Fluid. Mech.*, 121:43–58, 1982.

[9] Mudit K. Jain, Roxanne Richman, Jed Crowe, Patrick D. Wolf, and Ben Pless. Effect of fat layer on epicardial radiofrequency lesions. *Pacing. Clin. Electrophysiol.*, 2000. NASPE Abstracts.

[10] Mudit K. Jain and Patrick D. Wolf. Temperature-Controlled and Constant-Power Radio-Frequency Ablation: What affects Lesion Growth. *IEEE Trans. Biomed. Eng.*, 46(12):405–412, December 1999.

[11] Mudit K. Jain and Patrick D. Wolf. A three-dimensional finite element model of radiofrequency ablation with blood flow and its experimental validation. *Annals of Biomedical Engineering*, 28(9):1075–1084, 2000.

[12] Claes Johnson. *Numerical solution of partial differential equations by the finite element method*. Cambridge University Press, Cambridge, 1995.

[13] Krishna Kharge, Thomas Deneke, Helmut Haardt, Bernd Lemke, Peter Grewe, Klaus-Michael Müller, and Alex Laczkovics. Saline-irrigated, cooled-tip radiofrequency ablation is an effective technique to perform the Maze procedure. *Ann. Thorac. Surg.*, 72:S1090–1095, 2001.

[14] Sylvian Labonté. A computer simulation of radio-frequency ablation of the endocardium. *IEEE Trans. Biomed. Eng.*, 41(9):883–890, September 1994.

[15] Sylvian Labonté. Numerical model for radio-frequency ablation of the endocardium and its experimental validation. *IEEE Trans. Biomed. Eng.*, 41(2):108–115, February 1994.

[16] Albert C. Lin and David Wilbur. Complications associated with radiofrequency catheter ablation. In *Radiofrequency Catheter Ablation of Cardiac Arrhythmias: Basic Concepts and Clinical Applications*, pages 737–746. Futura Publishing Company Inc., Armonk, New York 10504, 2000.

[17] Ian D. McRury, Dorin Panescu, Mark A. Mitchell, and David E. Haines. Nonuniform heating during radiofrequency catheter ablation with long electrodes: monitoring the edge effect. *Circulation*, 11:4057–4064, December 1996.

[18] Xiaoyi Min and Rahul Mehra. Analysis of the variables that affect electrode and tissue temperature during RF ablation in a finite element analysis model. In *Computers in Cardiology*, pages 205–208. IEEE, 1999.

[19] H. Nakagawa, W. S. Yamanashi, J. V. Pitha, M. Arruda, X. Wang, K. Ohtomo, K. J. Beckman, J. H. McClelland, R. Lazzara, and W. M. Jackman. Arrhythmias/radiofrequency ablation: Comparison of in vivo tissue temperature profile and lesion geometry for radiofrequency ablation with a saline-irrigated electrode versus temperature control in a canine thigh muscle preparation. *Circulation*, 91(8):2264–73, April 1995.

[20] Dorin Panescu, James G. Whayne, Sidney D. Fleischman, Mark S. Mirotznik, David K. Swanson, and John G. Webster. Three-Dimensional Finite Element Analysis of Current Density and Temperature Distributions During Radio-Frequency Ablation. *IEEE Trans. Biomed. Eng.*, 42(9):879–890, September 1995.

[21] Helen H. Petersen, Jesper H. Svendsen, Stig Haunsø, and Douglas L. Packer. Irrigated tip radiofrequency ablation: Is there a virtual electrode effect? *Pacing. Clin. Electrophysiol.*, page 821, April 1999. NASPE Abstracts.

[22] Y. Saad and M. H. Schultz. GMRES: A generalized minimal residual algorithm for solving nonsymmetric linear systems. *SIAM J. Sci. Statist. Comput.*, 7:856–869, 1986.

[23] J. Schöberl. NETGEN – An advancing front 2D/3D-mesh generator based on abstract rules. *Comput. Visual. Sci*, 1:41–52, 1997.

[24] Herman P. Schwan and Kenneth R. Foster. RF–Field Interactions with Biological Systems: Electrical Properties and Biophysical Mechanisms. *Proc. IEEE*, 68(1):104–113, January 1980.

[25] Lisa L. Skrumeda and Rahul Mehra. Comparison of standard and irrigated radiofrequency ablation in the canine ventricle. *J. Cardiovasc. Electrophysiol.*, 9(11):1196–205, November 1998.

[26] Eduardo Sosa, Mauricio Scanavacca, André D'Avila, João Piccioni, Osvaldo Sanchez, José L. Velarde, Marcio Silva, and Basileo Reolão. Endocardial and epicardial ablation guided by nonsurgical transthoracic epicardial mapping to treat recurrent ventricular tachycardia. *J. Cardiovasc. Electrophysiol.*, 9(3):229–239, March 1998.

[27] A. Surowiec, S. S. Stuchly, L. Eidus, and A. Swarup. *In vitro* dielectric properties of human tissues at radiofrequencies. *Phys. Med. Biol.*, 32(5):615–621, 1987.

[28] Supan Tungjitkusolmun, Victor R. Vorperian, Naresh Bhavaraju, Hong Cao, Jang-Zern Tsai, and John G. Webster. Guidelines for predicting lesion size at common endocardial locations during radio-frequency ablation. *IEEE Trans. Biomed. Eng.*, 48(2):194–201, February 2001.

[29] Wai Shun Wong, Brian A. WanderBrink, Richard E. Riley, Mark Pomeranz, Mark S. Link, Munther K. Homoud, N. A. Mark Estes III, and Paul J. Wang. Effect of saline irrigation flow rate on temperature profile during cooled radiofrequency ablation. *J. Interv. Card. Electrophysiol.*, 4:321–326, 2000.